crystals

MDPI

Article

Superhydrophobic, Corrosion-Resistant ORMOSIL Coating on 6061 Aluminum Alloy for Aviation Fuel Environments

Xiang Liu [1], Huijie Sun [1], Jiaxing Ru [1], Xiao Hu [1], Rui Lu [1], Yumo Wang [1], Lei Zhang [1] and Hengcheng Wan [1,2,*]

[1] Civil Aircraft Fire Science and Safety Engineering Key Laboratory of Sichuan Province, Civil Aviation Flight University of China, Guanghan 618300, China; liux710@163.com (X.L.); sunhuijie1009@163.com (H.S.); jiaxingru00@163.com (J.R.); 17365585176@163.com (X.H.); lynn5544@126.com (R.L.); eightshn@163.com (Y.W.); leizhang@cafuc.edu.cn (L.Z.)

[2] College of Smart Energy, Shanghai Jiao Tong University, Shanghai 200240, China

* Correspondence: wanhc@cafuc.edu.cn

Abstract

During aviation operations, low temperatures can cause fuel freezing and icing on 6061 aluminum fuel lines, threatening flight safety. To mitigate this, a surface treatment combining $FeCl_3$ etching and an ORMOSIL sol–gel coating was proposed to construct a superhydrophobic functional layer. $FeCl_3$ etching generated a hierarchical micro/nanostructure on the aluminum surface, while the ORMOSIL layer, formed by the co-hydrolysis and condensation of PFOTES and HDTMS, built Si-O-Si networks and introduced C-F groups to reduce surface energy and enhance stability. The modified surface showed a high water contact angle of 161.44°, confirming excellent superhydrophobicity. AFM analysis revealed a significant increase in surface roughness (Sa = 0.844 μm), confirming the formation of a hierarchical micro/nanostructure. Electrochemical measurements showed a positive shift in corrosion potential from −0.723 V to −0.652 V, demonstrating enhanced corrosion resistance. More importantly, after 120 h of immersion in aviation fuel, the coating maintained a high contact angle of 156.73° and preserved its Si-O-Si network and fluorinated functional groups, confirming outstanding fuel resistance and long-term stability. These results demonstrate that the proposed ORMOSIL coating is a promising protective strategy for aviation fuel systems operating under low-temperature and corrosive conditions.

Keywords: superhydrophobic; fluorosilane; micro/nano hierarchical structure; aviation fuel; sol–gel method

1. Introduction

During high-altitude flight, aircraft are frequently exposed to extremely low temperatures and high humidity, with ambient temperatures often falling below the freezing point [1]. Under such conditions, low temperatures can cause condensed water droplets to freeze on the inner walls of aluminum alloy pipelines connecting the fuel tank to the engine, potentially leading to blockage [2]. The formation of ice layers can narrow the effective cross-section of the pipelines, increase flow resistance and the risk of blockage, and disrupt the stable delivery of fuel, thereby compromising the operational safety of the propulsion system. Prolonged exposure to low temperatures may also exacerbate inner-surface icing and frost accumulation on components, leading to interruption of fuel supply and posing a substantial threat to flight safety [3]. To address these challenges, constructing superhydrophobic surfaces has emerged as an effective surface protection strategy [4]. Such surfaces significantly reduce the contact area between water droplets

Check for updates

Academic Editor: Jan Macutkevic

Received: 7 June 2026
Revised: 2 July 2026
Accepted: 5 July 2026
Published: 10 July 2026

Copyright: © 2026 by the authors. Licensee MDPI, Basel, Switzerland. This article is an open access article distributed under the terms and conditions of the Creative Commons Attribution (CC BY) license.

and solid substrates, thereby weakening liquid adhesion [5]. Wettability is one of the most important surface characteristics governing the interaction between a solid surface and liquids. It is commonly evaluated by the water contact angle (CA), which reflects the degree of spreading of a water droplet on a surface. Generally, surfaces with contact angles lower than 90° are considered hydrophilic, whereas those with contact angles greater than 90° are regarded as hydrophobic. When the contact angle exceeds 150° and the sliding angle remains below 10°, the surface is classified as superhydrophobic [6]. Surface wettability is strongly influenced by both surface chemistry and surface roughness. According to the Wenzel and Cassie–Baxter wetting models, hierarchical micro/nanostructures combined with low-surface-energy materials can effectively trap air pockets at the solid–liquid interface, thereby reducing liquid adhesion and enhancing water repellency. These wetting characteristics are particularly important for aircraft fuel systems, where reduced water adhesion, delayed ice nucleation, and enhanced corrosion resistance are essential for maintaining operational safety under low-temperature environments. Among various coating materials, organically modified silicates (ORMOSILs) offer an ideal platform for the fabrication of superhydrophobic surfaces due to their excellent chemical resistance, thermal stability, mechanical robustness, and inherently low surface energy [7]. When applied to the surface of aerospace-grade aluminum alloys, ORMOSIL coatings demonstrate promising durability and environmental adaptability, providing an effective protective solution for critical components in aircraft fuel delivery systems [8]. Smitha [9] developed an ORMOSIL-ZrO_2 hybrid nanocomposite coating by combining methyltrimethoxysilane (MTMS) and glycidyloxypropyl trimethoxysilane (GPTMS) as organosilane precursors with zirconium isopropoxide (ZIP) as the inorganic nano-dispersed phase. Electrochemical tests conducted in 3.5 wt% NaCl solution revealed that the coated aluminum alloy exhibited a significantly reduced corrosion current density of 10^{-7} A/cm^2 and a polarization resistance as high as 10^5 Ω·cm^2, demonstrating excellent corrosion resistance. Metroke [10] fabricated ORMOSIL coatings on 2024-T3 aluminum alloy substrates. Electrochemical tests showed that the coatings exhibited high polarization resistance and impedance modulus, confirming their excellent protective performance for aluminum substrates and long-term stability in corrosive environments.

As a commonly used material in fuel systems, 6061 aluminum alloy has drawn attention for surface modification aimed at improving its anti-icing and corrosion resistance [11,12]. Although progress has been made in the fabrication of superhydrophobic surfaces, challenges remain in achieving structurally stable and functionally durable coatings for key areas within aviation fuel systems [13,14]. In this study, a hierarchical micro/nano-structured surface was fabricated on 6061 aluminum alloy via $FeCl_3$ etching, followed by the deposition of an ORMOSIL coating derived from 1H,1H,2H,2H-perfluorooctyltriethoxysilane (PFOTES) and hexadecyltrimethoxysilane (HDTMS). The resulting composite surface exhibited both superhydrophobicity and excellent corrosion resistance [15,16]. The performance and applicability of this surface treatment were systematically evaluated under aviation-relevant conditions, offering a promising protective strategy to enhance the environmental resilience and operational safety of aircraft fuel systems. The hydrolysis and condensation of PFOTES and HDTMS, as well as the proposed ORMOSIL siloxane network, are schematically illustrated in Figure 1.

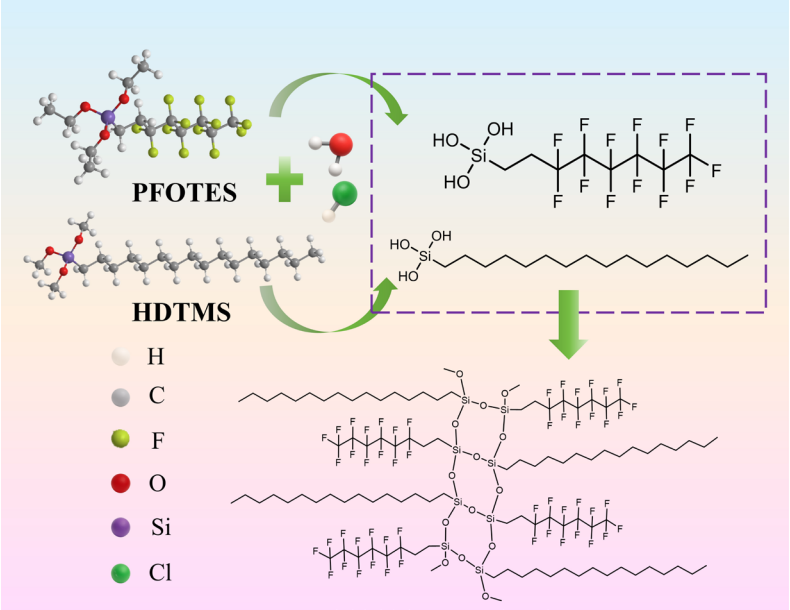


Figure 1. Schematic illustration of the hydrolysis and condensation of PFOTES and HDTMS to form the ORMOSIL siloxane network.

2. Materials and Methods

2.1. Experimental Material

The substrate material used in this study was aerospace-grade 6061 aluminum alloy, which is widely used in aerospace structures and fuel system components because of its favorable strength-to-weight ratio, corrosion resistance, and machinability [17]. Its nominal composition was Al > 96%, Si < 0.8%, Fe < 0.7%, Cu < 0.4%, Mg < 1.2%, Mn < 0.15%, Cr < 0.35%, Zn < 0.25%, and Ti < 0.15%. The chemicals utilized included ferric chloride hexahydrate (AR grade, Shanghai Titan Technology Co., Ltd., Shanghai, China), 1H,1H,2H,2H-perfluorooctyltriethoxysilane (PFOTES, RG grade, Shanghai Titan Technology Co., Ltd., China), hexadecyltrimethoxysilane (HDTMS, RG grade, Shenzhen Zhongfu Technology Co., Ltd., Shenzhen, China), methanol (BASIC HPLC grade, Shanghai Titan Technology Co., Ltd., China), ethanol (HPLC grade, Shanghai Titan Technology Co., Ltd., China), petroleum ether (AR grade, Shanghai Titan Technology Co., Ltd., China), and jet fuel (Maoming Yuanmao Petrochemical Co., Ltd., Maoming, China).

2.2. Experimental Equipment

The main experimental equipment used in this study included an electric heating sleeve, an oven, an ultrasonic cleaning instrument, and beakers. The electric heating sleeve (Shanghai Lichen Bangxi Instrument Technology Co., Ltd., Shanghai, China) was employed for temperature-controlled heating during the preparation process. The oven (Shanghai Shanzhi Instrument Equipment Co., Ltd., Shanghai, China) was used for drying and thermal curing of the samples. The ultrasonic cleaning instrument (Shanghai Yixin Electronic Technology Co., Ltd., Shanghai, China) was used to clean the aluminum alloy substrates before surface treatment. Beakers (Sichuan Shuniu Horticulture Co., Ltd., Chongzhou, China) were used for solution preparation, substrate immersion, and sample treatment.

2.3. Experimental Characterization Methods

The surface wettability of the samples was evaluated using a water contact angle test, with a measurement range of 0–180° and an accuracy of ±0.1°. For each sample group, measurements were taken three times at five different positions, and the average value was used to reflect the overall hydrophobic performance. Surface morphology was observed

using a field-emission scanning electron microscope (SEM) (Carl Zeiss Microscopy GmbH, Jena, Germany) with an accelerating voltage of 10 kV, a working distance of 5.5 mm, and a magnification range from 20,000 to 100,000×. Elemental composition and distribution were analyzed using energy-dispersive spectroscopy (EDS) (Oxford Instruments, Abingdon, UK) in conjunction with SEM. Atomic force microscopy (AFM) (Billerica, Billerica, USA) was employed to analyze the microstructure of the surface, with a scan area of 3 μm × 3 μm. Arithmetic mean roughness (Sa) and root mean square roughness (Sq) were extracted for quantitative evaluation. The surface chemical states were analyzed using X-ray photoelectron spectroscopy (XPS) (Thermo Fisher Scientific, Waltham, USA), with a scanning energy range of 0–1200 eV. Fourier-transform infrared spectroscopy (FTIR) (Thermo Fisher Scientific, Waltham, USA) was conducted over the range of 400–4000 cm^{-1} to detect the vibrational frequencies of chemical bonds and obtain characteristic absorption peaks. The corrosion resistance of the samples was analyzed using an electrochemical workstation through potential–current curves, with a scan rate of 0.5 mV/s and a potential range of open-circuit potential (EOCP) ±100 mV.

2.4. Experimental Process

First, the 6061 aluminum alloy samples were sequentially immersed in 99.9% methanol, 99.5% ethanol, petroleum ether, and deionized water, with each step involving 15 min of ultrasonic cleaning to remove surface oils and impurities. The cleaned samples were then immersed in a 15 wt% $FeCl_3$ solution and chemically etched at 40 °C for 10 min. After etching, the samples were again ultrasonically cleaned with methanol to remove residual $FeCl_3$ and reaction byproducts and subsequently dried under a nitrogen stream to ensure complete surface dryness. Next, the ORMOSIL sol–gel solution was prepared using PFOTES (98%) and HDTMS (5%) as organosilane precursors. Ethanol, deionized water, and 37% hydrochloric acid were added according to the molar ratio of Precursor: EtOH:H_2O:HCl = 1:856:7.2:0.9, and the mixture was vigorously stirred for 2 min to promote hydrolysis and condensation reactions. The prepared sol was then applied onto the etched aluminum alloy surface at room temperature using dip coating.

During $FeCl_3$ treatment, the aluminum surface underwent a redox-assisted chemical etching process. Fe^{3+} acted as an oxidizing agent and promoted the dissolution of metallic Al, while Fe^{3+} was reduced to Fe^{2+}. The main reactions can be expressed as follows:

$$Al \rightarrow Al^{3+} + 3e^{-}$$

$$3Fe^{3+} + e^{-} \rightarrow Fe^{2+}$$

$$Al + 3FeCl_3 \rightarrow AlCl_3 + 3FeCl_2$$

In addition, Cl^{-} ions could locally disrupt the native aluminum oxide layer and promote pitting corrosion, resulting in the formation of micro-scale pits and hierarchical rough structures on the aluminum alloy surface.

After deposition, the samples were first heat-treated at 60 °C for 30 min to remove residual solvent, followed by heating at 120 °C for 60 min to complete curing of the coating. Upon cooling, ORMOSIL composite coatings with superhydrophobic properties were successfully obtained. The chemical etching process followed by the deposition of the ORMOSIL coating is schematized in Figure 2.

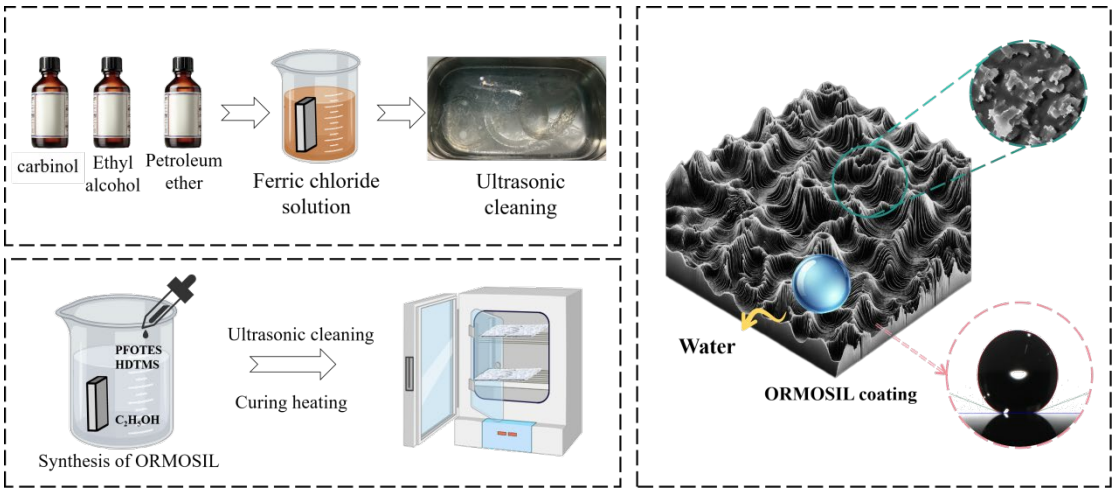


Figure 2. Illustration of the experimental procedure.

3. Results

To evaluate the effectiveness of surface modification and confirm the formation of the ORMOSIL coating, energy-dispersive spectroscopy (EDS) was conducted to analyze the surface elemental composition of the aluminum alloy samples before and after treatment [18]. As shown in Figure 3a, the untreated aluminum alloy primarily exhibited strong signals of aluminum (Al) and carbon (C). According to the elemental total spectrum measured by EDS, aluminum, as the main component of the substrate, accounted for 87.51 wt%, whilecarbon accounted for 11.20 wt%, which may be derived from residual organic matter frommechanical processing or pollutants adsorbed from the environment. Minor signals of oxygen (O) and fluorine (F) were also detected, which can be attributed to the native oxide layer and trace environmental fluorine species [19]. At this stage, no silicon (Si) signal was observed, indicating the absence of any silane-based hybrid coating on the surface. After $FeCl_3$ etching and deposition of the ORMOSIL sol–gel coating, significant changes in surface composition were observed. The Al signal was greatly reduced, suggesting that a coating layer had formed and that the underlying Al signal was further attenuated by the micro/nanostructures generated by etching [20]. The carbon content increased to 12.38 wt%, primarily due to the long alkyl chains introduced by HDTMS, which help establish a low-surface-energy coating. The oxygen content rose to 2.23 wt%, likely due to the hydrolysis and condensation of the silane precursors and the formation of Al-OH groups during the etching process. The fluorine content reached 2.17 wt%, originating from the $-CF_3$ and $-CF_2-$ groups in PFOTES, which are crucial for imparting superhydrophobic properties. Silicon, which was previously undetectable, appeared at 0.54 wt% after modification, confirming the successful formation of a siloxane-based hybrid network derived from the hydrolyzed PFOTES and HDTMS [21]. Overall, the significant reduction in Al content and the marked increase in non-metallic elements such as C, O, F, and Si after modification indicate the successful construction of an organic–inorganic hybrid ORMOSIL functional coating on the aluminum alloy surface, effectively enhancing the surface composition and functional performance of the material [22].

To further investigate the elemental composition and chemical states of the sample surfaces, X-ray photoelectron spectroscopy (XPS) was conducted on untreated aluminum alloy, etched samples, and ORMOSIL-modified samples [23]. As shown in Figure 3b, the wide-scan XPS spectrum of the untreated 6061 aluminum alloy reveals the presence of O 1s, C 1s, and Al 2p peaks, indicating that the surface mainly consists of oxygen, carbon, and aluminum. The O 1s peak is attributed to the naturally formed oxide layer on the aluminum surface, while the C 1s peak likely originates from organic contaminants

adsorbed from the ambient environment [24]. The presence of the Al 2p signal suggests that the oxide layer is relatively thin, allowing photoelectrons from the aluminum substrate to be detected [25]. Overall, the untreated sample exhibits the typical surface composition of metallic aluminum [26]. After surface modification, the XPS wide-scan spectrum of the sample is shown in Figure 3c. In addition to the original O 1s, C 1s, and Al 2p peaks, new signals corresponding to F 1s, Cl 2p, and Si 2p are observed. The prominent F 1s peak confirms the successful incorporation of fluorine, mainly derived from the fluorocarbon chains in PFOTES [27]. The presence of the Si 2p peak indicates the formation of a siloxane-based network structure [28]. The Cl 2p signal may originate from residual $FeCl_3$ used during etching or from reaction by-products [29]. Compared to the untreated sample, the Al 2p signal is significantly weakened, suggesting that the modified coating forms a more complete coverage on the surface; however, the remaining signal also indicates that the film is thin enough for some photoelectrons from the substrate to escape. This indicates the successful incorporation of fluorocarbon groups and siloxane structures into the ORMOSIL coating, as well as a significant enhancement in surface coverage on the aluminum alloy.

To further elucidate the chemical bonding states within the ORMOSIL coating, high-resolution XPS analysis was performed on the Si 2p and C 1s orbitals, as shown in Figure 3d,e. In the Si 2p spectrum (Figure 3d), three characteristic peaks were observed at binding energies of 101.70 eV, 102.90 eV, and 104.12 eV. The component at 101.70 eV is assigned to Si-O-C/SiOxCy-related species derived from partially hydrolyzed or organically modified silane structures, rather than Si-C bonds. The peak at 102.90 eV is attributed to Si-O-Si bonds in the siloxane network, while the component at 104.12 eV is associated with residual Si-OH or highly oxidized silicon species. In the C 1s high-resolution spectrum (Figure 3e), a strong peak at 284.8 eV corresponds to C-C/C-H bonds, while peaks at 290.6 eV and 292.8 eV are associated with CF_2-CF_2 and CF_3-CF_2 structures, respectively [30]. No distinct C 1s component near 283 eV was observed; therefore, the presence of Si-C bonds cannot be confirmed from the C 1s spectrum. These fluorinated features originate from the functional groups of PFOTES, and their strong signals indicate surface enrichment of fluorine-containing species. According to studies, the critical surface tensions of -CF_2 and -CF_3 groups are approximately 23 mN/m and 15 mN/m, respectively—which are much lower than those of conventional hydrocarbon groups such as -CH_2 and -CH_3 [31]. This surface fluorination plays a crucial role in lowering the surface free energy, which directly contributes to the excellent hydrophobic performance observed in subsequent contact angle measurements. Together, the XPS results confirm the successful formation of a hybrid organic–inorganic ORMOSIL network on the aluminum alloy surface, where the fluorinated moieties and siloxane backbone synergistically enhance the coating's environmental durability and superhydrophobic properties, providing a solid structural and functional foundation for applications in aircraft fuel systems [32].

Figure 3f,g present the Fourier-transform infrared (FTIR) spectra of the ORMOSIL-coated sample and the control specimens to analyze the functional group composition and structural characteristics of the coating. As shown in Figure 3f, both the untreated and ferric chloride-etched samples exhibit negligible absorption peaks across the spectral range, primarily due to the predominance of metal oxides and other inorganic species on their surfaces, which lack IR-active organic functional groups and therefore do not generate significant spectral responses [33]. In sharp contrast, the ORMOSIL-coated sample displays distinct absorption bands in multiple regions, indicating the successful incorporation of various organic and inorganic hybrid structures. To further elucidate these features, the magnified spectrum in Figure 3g reveals several characteristic peaks. The peaks observed at 1085 cm^{-1} [34], 1119 cm^{-1} [35], and 1189 cm^{-1} are attributed to the asymmetric stretching vibrations of the Si-O-Si network and the C-F stretching vibra-

tions of -CF_2 and -CF_3 groups [36], respectively, confirming the formation of a siloxane backbone and the introduction of fluorocarbon functionalities during the sol–gel process. Additionally, weaker absorption bands at 1444, 1365, and 1319 cm^{-1} correspond to the bending vibrations of C-H bonds from the long alkyl chains in PFOTES and HDTMS, as well as partial C-F skeletal vibrations [37]. These long hydrophobic chains contribute to molecular-level water repellency, thereby enhancing the surface's hydrophobic character. The band at approximately 897 cm^{-1} is reassigned to Si-O-C, Si-O-Si bending, or residual alkoxy/silanol-related vibrations, rather than Si-C stretching. This reassignment is more consistent with the hydrolysis and condensation chemistry of PFOTES and HDTMS during ORMOSIL formation. The absorption at 694 cm^{-1} is attributed to the out-of-plane bending vibrations of C-H bonds, which may indicate the presence of ordered alkyl chain packing on the surface [38]. Taken together, these functional groups synergistically form a chemically stable hybrid network with intrinsically low surface energy The integration of fluorocarbon chains and siloxane structures significantly reduces the surface free energy, which is critical for achieving superior superhydrophobic performance [39]. This hybrid structure provides a solid theoretical and structural foundation for enhanced anti-icing, anti-corrosion, and self-cleaning functionalities under extreme service conditions.

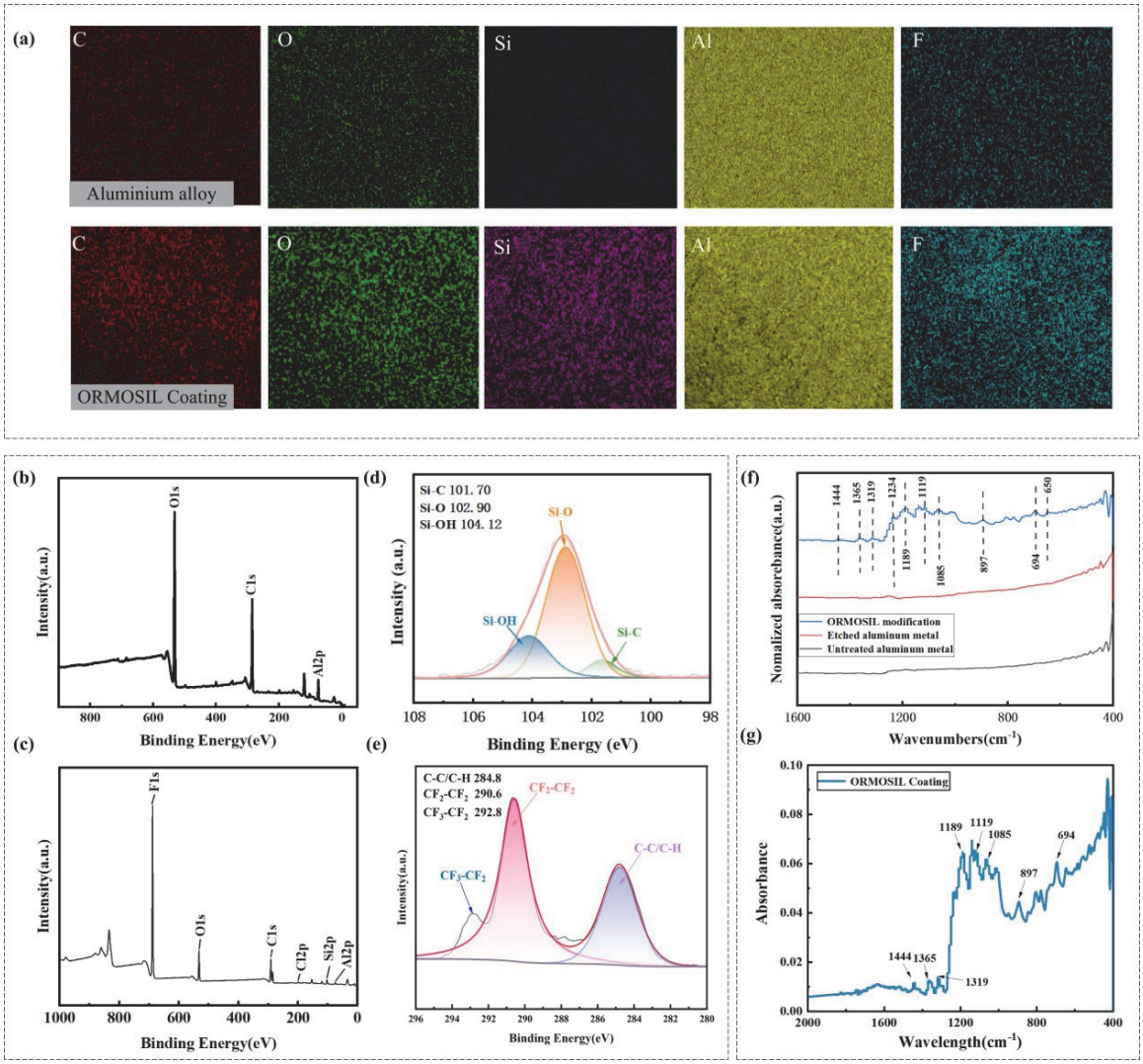


Figure 3. (**a**) EDS elemental mapping of aluminum alloy and ORMOSIL-coated samples; (**b**,**c**) XPS survey spectra; (**d**,**e**) High-resolution XPS spectra of Si 2p and C 1s; (**f**) FTIR spectrum; (**g**) magnified FTIR spectrum of the ORMOSIL coating.

Figure 4 presents SEM images of the coating surface at lower (5 μm scale bar) and higher (1 μm scale bar) magnification scales, respectively. Numerous fine particles can be observed on the rough micro/nanostructured surface. These images clearly reveal the morphological evolution from a relatively smooth surface to a hierarchically rough structure, demonstrating the significant regulatory effects of chemical etching and ORMOSIL modification on the surface microstructure. As shown in Figure 4a, the untreated aluminum surface appears relatively smooth. In the low-magnification SEM image with a scale bar of 5 μm, no noticeable structural features are observed aside from slight machining marks. In the corresponding high-magnification SEM image with a scale bar of 1 μm, the surface still lacks nanoscale features such as sharp protrusions or pores. The overall flat morphology and low surface roughness indicate an inability to stably trap air, which is unfavorable for forming an ideal superhydrophobic state. Following $FeCl_3$ etching, the surface morphology changes significantly, as shown in Figure 4b. In the low-magnification SEM image with a scale bar of 5 μm, a large number of uniformly distributed cubic microstructures appear across the surface, arranged in stacked lamellar formations with clear edges and high regularity. Further observation in the high-magnification SEM image with a scale bar of 1 μm reveals that these individual platelets exhibit well-defined boundaries and ordered vertical alignment, forming step-like terrace structures. These microstructures are the result of localized dissolution induced by $FeCl_3$, possibly aligned with specific crystallographic orientations of the aluminum substrate [40]. This localized dissolution was mainly caused by the redox reaction between Al and Fe^{3+}, accompanied by Cl^--induced disruption of the native oxide layer, which promoted anisotropic etching and pit formation. The formation of these micron-scale step-like and layered features greatly increases surface roughness and provides a suitable scaffold for the attachment of low-surface-energy materials [41]. On this basis, the introduction of the ORMOSIL coating leads to further morphological changes, as illustrated in Figure 4c. EDX analysis confirmed that the particles mainly consisted of Si, O, C, and F elements, suggesting that they originated from the ORMOSIL network rather than corrosion products or residual etching species. In the SEM image with a scale bar of 5 μm, the original cubic structures remain partially visible but are covered by numerous irregular granular deposits, suggesting that sol–gel reaction products have accumulated on the substrate [42]. In the high-magnification SEM image with a scale bar of 1 μm, these fine particles are seen to be uniformly distributed among the microstructures, forming a multiscale composite surface composed of particles, lamellae, and pores. This hierarchical roughness effectively promotes a Cassie–Baxter wetting regime, enabling water droplets to remain suspended on the air–solid composite interface, thereby significantly enhancing both the superhydrophobic and oleophobic properties of the surface [43].

To systematically evaluate the regulatory effects of different surface treatments on the microstructure of aluminum alloy, atomic force microscopy (AFM) was employed to characterize the surface topography, and two key parameters—arithmetic mean roughness (Sa) and root mean square roughness (Sq)—were extracted to quantitatively assess the evolution of surface roughness. As shown in Figure 4d, the untreated 6061 aluminum alloy surface exhibited a relatively smooth morphology, with Sa and Sq values of 0.212 μm and 0.185 μm, respectively. Upon $FeCl_3$ etching (Figure 4e), the AFM images revealed the emergence of densely stacked lamellar structures and pronounced etching pits, forming micron-scale terrace-like protrusions. These features are attributed to the localized dissolution of aluminum driven by crystallographic orientation-dependent reactivity with $FeCl_3$ [44]. The resulting increase in surface roughness provides favorable air entrapment sites and establishes the initial geometric framework necessary for the formation of a three-phase (solid–liquid–gas) interface, thereby laying a structural foundation for the construction of superhydrophobic coatings [45]. Following the subsequent deposition

of the ORMOSIL coating via sol–gel processing (Figure 4f), surface roughness increased further, with Sa and Sq values rising to 0.844 μm and 0.654 μm, respectively, nearly double those of the etched-only sample. The coating introduced numerous organic–inorganic hybrid clusters, generating densely distributed irregular particulate protrusions that formed a hierarchical multiscale roughness across the surface. This synergistically constructed micro/nanostructured topography greatly enhances the air-retention capacity beneath water droplets, effectively reducing the actual contact area between the liquid and solid phases [46,47]. As a result, the surface remains in a stable gas–solid composite state, significantly improving its superhydrophobicity. More importantly, the enhanced roughness endows the surface with the ability to maintain the Cassie–Baxter state even under extreme conditions such as high humidity and low temperature [48]. The corresponding quantitative roughness parameters obtained from the AFM analysis are summarized in Table 1.

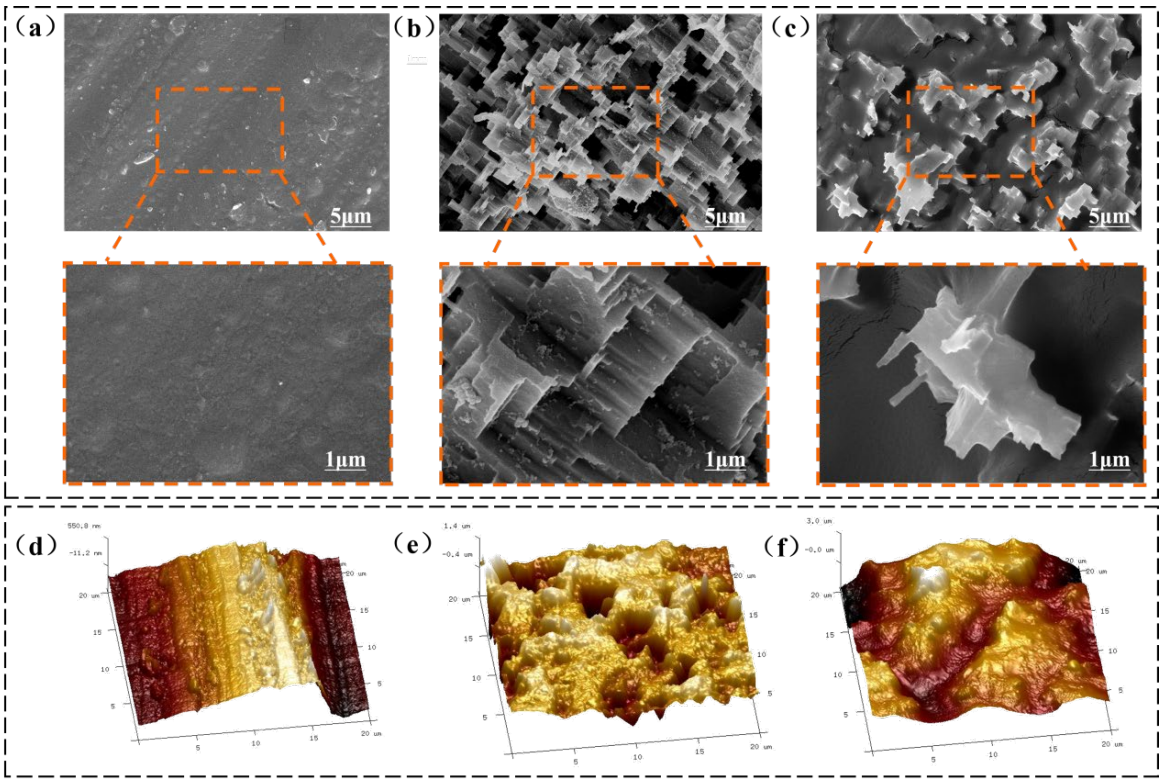


Figure 4. (**a**–**c**) SEM images of aluminum alloy, $FeCl_3$-etched aluminum alloy, and the ORMOSIL-coated surface; (**d**–**f**) AFM 3D topography images of aluminum alloy, $FeCl_3$-etched aluminum alloy, and the ORMOSIL-coated surface.

Table 1. Sa and Sq values of aluminum alloy surfaces with different treatments.

	Aluminum Alloy Surface	$FeCl_3$ Etching	ORMOSIL Coating
sa (μm)	0.212	0.479	0.844
sq (μm)	0.185	0.359	0.654

The contact angle quantitatively reflects the wettability of a solid surface by a liquid [49]. Figure 5a–c schematically illustrates the wetting behavior of water droplets on aluminum alloy surfaces before and after each treatment step, with representative contact angle values labeled to demonstrate the trend of wettability change. Specifically, the untreated 6061 aluminum alloy surface exhibits a contact angle of 74.34°, primarily due to its smooth morphology and high surface energy, which promotes strong interfacial

adhesion between water droplets and the solid surface [50]. After $FeCl_3$ etching (Figure 5b), the contact angle decreases to 47.35°, indicating enhanced wettability. This is attributed to the increased surface roughness and lamellar microstructures formed during etching, which, in the absence of low-energy functional groups, promote liquid infiltration into the grooves—typical of the Wenzel wetting regime [51]. In contrast, the ORMOSIL-coated sample (Figure 5c) shows a contact angle of 161.44°, reflecting a transition to a superhydrophobic state. This is the result of the synergistic combination of hierarchical surface roughness and the low surface energy introduced by the fluorinated alkyl chains of PFOTES in the ORMOSIL layer [52]. These features enable the Cassie–Baxter wetting state, in which air pockets are trapped beneath the droplet, significantly reducing solid–liquid contact and resulting in high water mobility and low adhesion [52,53]. To improve the reliability of the tests and minimize random errors, each sample group was measured at five different positions, with three repeated measurements at each position, resulting in a total of 15 contact angle data points. Figure 5d presents the average contact angles and standard deviations for each group: 73.34° for untreated aluminum, 47.13° after $FeCl_3$ etching, and 159.85° after ORMOSIL coating [54].

To evaluate the electrochemical corrosion performance of aluminum alloy under different surface treatments, potentiodynamic polarization tests were carried out in 3.5 wt% NaCl solution, and the results are shown in Figure 5e. The untreated aluminum alloy exhibited a corrosion potential of −0.723 V and a corrosion current density of 3.48×10^{-8} A/cm^2, indicating a relatively low corrosion rate under unprotected conditions, though the surface remained vulnerable to corrosion activation. After $FeCl_3$ etching, the corrosion potential shifted positively to −0.657 V, which implies a thermodynamic improvement. However, the corrosion current density increased sharply to 1.00×10^{-5} A/cm^2 due to the formation of microstructural defects and discontinuities that significantly increased the specific surface area and reactivity. These features promoted localized corrosion processes and accelerated anodic dissolution, revealing that etching alone does not provide sufficient protection [55]. The sample treated with both $FeCl_3$ etching and ORMOSIL coating showed the most positive corrosion potential at −0.652 V, reflecting the highest thermodynamic stability among the three samples. Although its corrosion current density reached 5.66×10^{-6} A/cm^2, slightly higher than that of the untreated alloy, it was markedly lower than the etched sample. This result demonstrates that, while the underlying etched structure may still contribute to surface activity, the ORMOSIL coating effectively suppresses corrosion [56]. The coating features a densely cross-linked Si-O-Si network and abundant fluorinated groups, which act together to block the ingress of water and chloride ions and reduce surface energy [57]. Overall, the ORMOSIL-coated aluminum alloy achieved a favorable balance between corrosion potential and corrosion current density, demonstrating a synergistic enhancement in both thermodynamic and kinetic corrosion resistance. This surface modification strategy provides a robust and practical approach for protecting aluminum alloy components in aggressive environments, particularly in the context of aviation fuel systems.

Figure 5f presents the low-temperature stability test of the ORMOSIL-coated samples conducted at −10 °C, −20 °C, and −30 °C. Water droplets were deposited onto the coated surfaces, and images were captured every 20 s during a 100 s observation period to monitor changes in surface morphology and appearance under freezing conditions, thereby evaluating the coating's structural integrity and stability at low temperatures. Under all three temperature conditions, the droplets initially maintained a stable hemispherical shape without any immediate signs of crystallization or phase transition. However, between 60 and 80 s, changes in droplet transparency and contour deformation were observed, indicating the onset of ice nucleation. The similar freezing onset time observed at all

temperatures suggests that the ORMOSIL coating maintained its wetting properties and structural integrity under subzero conditions without noticeable degradation or failure. This demonstrates the coating's excellent low-temperature durability, as it retained its micro/nanostructure and fluorinated low-surface-energy characteristics even in severe cold environments. Although the coating could not completely prevent icing, the synergistic effects of the surface micro/nanostructures and fluorinated functional groups contributed to reducing heat transfer efficiency and suppressing ice nucleation at the solid–liquid interface [58]. The dynamic process of droplet behavior at low temperatures is provided in the Supplementary Video.

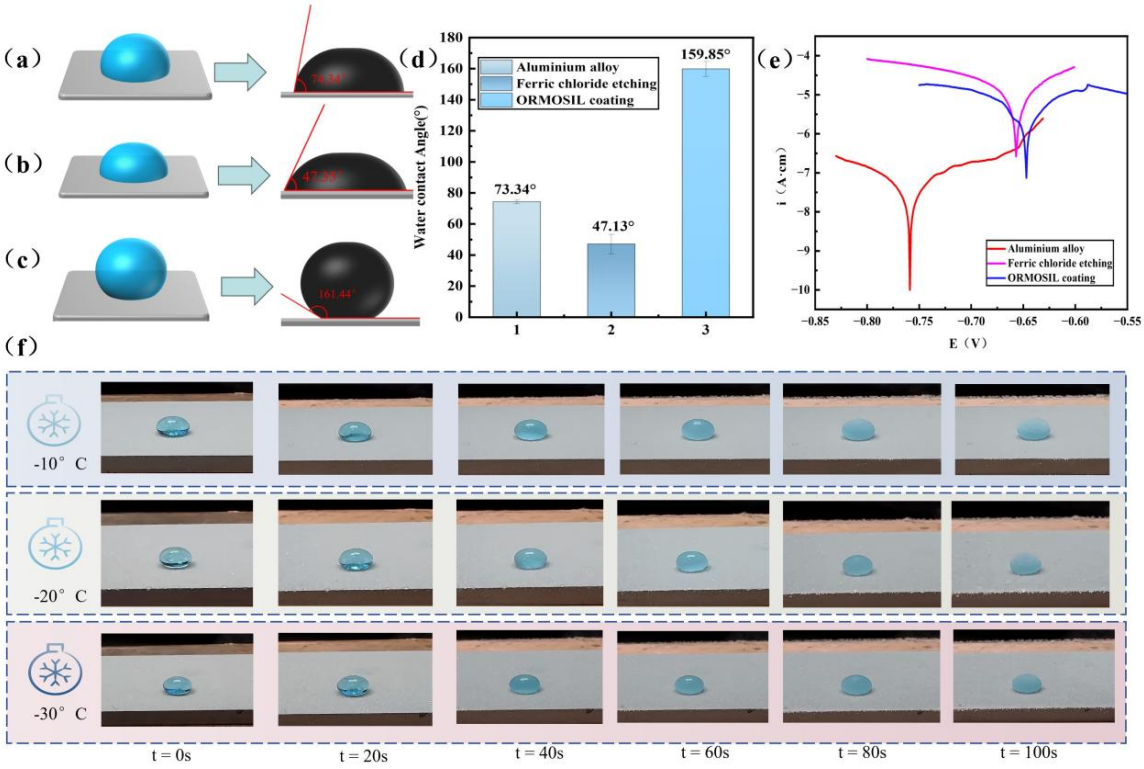


Figure 5. (**a**–**c**) Water contact angle images and measured values on aluminum alloy surfaces under different treatment conditions; (**d**) Bar chart of average water contact angles; (**e**) Potentiodynamic polarization curves; (**f**) Time-lapse images of icing-delay tests on ORMOSIL-coated samples at −10 °C, −20 °C, and −30 °C.

Under typical conditions, superhydrophobic coatings are prone to failure in jet fuel environments [59]. Active components in jet fuel can chemically react with or physically erode the coating surface, weakening its surface structure and low-surface-energy characteristics, thereby reducing its hydrophobic performance [60]. This degradation is especially pronounced under prolonged immersion and frequent contact, where the micro/nanostructures and hydrophobic functional groups of the coating are more likely to be damaged [61]. Therefore, this study systematically evaluated the coating's structural integrity and performance after jet fuel immersion to assess its stability and application potential. Detailed information on the jet fuel used for the immersion tests is provided in the Supplementary Materials.

Figure 6a evaluates the wetting durability of the ORMOSIL superhydrophobic coating after immersion in jet fuel. The results show that even after immersion, the coating maintains a high water contact angle of 156.73°, indicating excellent superhydrophobic performance [62,63]. To further assess its fuel resistance, continuous immersion tests were conducted to simulate the challenges encountered in real-world applications [64,65]. As

shown in Figure 6b, the contact angle showed a slight decreasing trend after 24 h, 48 h, 72 h, 96 h, and 120 h of immersion, but the coating still maintained good superhydrophobicity even after 120 h. This demonstrates the coating's excellent chemical stability and resistance to fuel corrosion, highlighting its potential for use in aviation and other long-term fuel exposure environments, and providing a solid foundation for further optimization and practical deployment [65].

Figure 6c shows the EDS elemental composition of the ORMOSIL coating after jet fuel immersion. The results reveal that the surface remains mainly composed of Al, C, O, F, and Si, consistent with the original coating state. Aluminum, as the substrate's primary element, accounts for 83.38 wt%. Compared with the pre-immersion condition (Figure 3a), the contents of carbon and fluorine remain stable at 13.60 wt% and 0.94 wt%, respectively, indicating no significant degradation of the hydrophobic functional groups. Notably, silicon is still detectable at 0.33 wt%, confirming that the siloxane network remains largely intact in the fuel environment, demonstrating good chemical stability and structural integrity of the coating [66]. Figure 6d presents the XPS survey spectrum of the immersed sample, clearly showing the continued presence of key elements such as Si, O, C, and F, which indicates that the chemical composition of the coating remains stable. Figure 6e displays the high-resolution Si 2p spectrum, showing binding states corresponding to Si-O-Si, Si-O-C/SiO_xC_y-related species, and a small amount of Si-OH, confirming that the organic–inorganic hybrid structure remains largely undamaged in the jet fuel environment and exhibits excellent chemical stability [67].

To further investigate the chemical structure changes after immersion, FTIR spectroscopy was conducted, as shown in Figure 6f. The absorption peak at 1639 cm^{-1} corresponds to O-H bending vibrations; peaks at 1445, 1358, and 1314 cm^{-1} correspond to C-H bending vibrations, indicating that the long alkyl chains introduced by HDTMS remain intact, which helps maintain surface hydrophobicity [68,69]. Peaks at 1234 and 1138 cm^{-1} are assigned to the asymmetric stretching of C-F bonds, confirming the stability of -CF_2 and -CF_3 groups, which are essential for maintaining low surface energy [70]. Peaks at 1116, 1064, and 1015 cm^{-1} correspond to Si-O-Si stretching vibrations, verifying the integrity of the siloxane framework [71]. Additionally, the bands at approximately 895 and 804 cm^{-1} are assigned to Si-O-C, Si-O-Si bending, or residual alkoxy/silanol-related vibrations, confirming that the siloxane-based ORMOSIL network was retained after jet fuel immersion.

To evaluate the microstructural stability under jet fuel conditions, SEM and AFM analyses were conducted, as shown in Figure 6g,h. In Figure 6g, the coating retains clear lamellar and particulate micro/nanostructures with no visible damage or delamination, indicating good adhesion and morphological integrity [72]. Figure 6h shows the 3D surface morphology, with an arithmetic average roughness of 0.679 μm and a root mean square roughness of 0.858 μm. These values confirm the continued presence of micro/nanoscale surface undulations, with no signs of collapse or smoothing. This multiscale roughness is beneficial for maintaining the Cassie–Baxter wetting state, which supports the superhydrophobic effect and ensures excellent water repellency in complex fuel environments [73]. As shown in Figure 6i, the corrosion current was determined to be 5.650×10^{-7} A, further confirming that the ORMOSIL coating retains good corrosion resistance after fuel immersion [74].

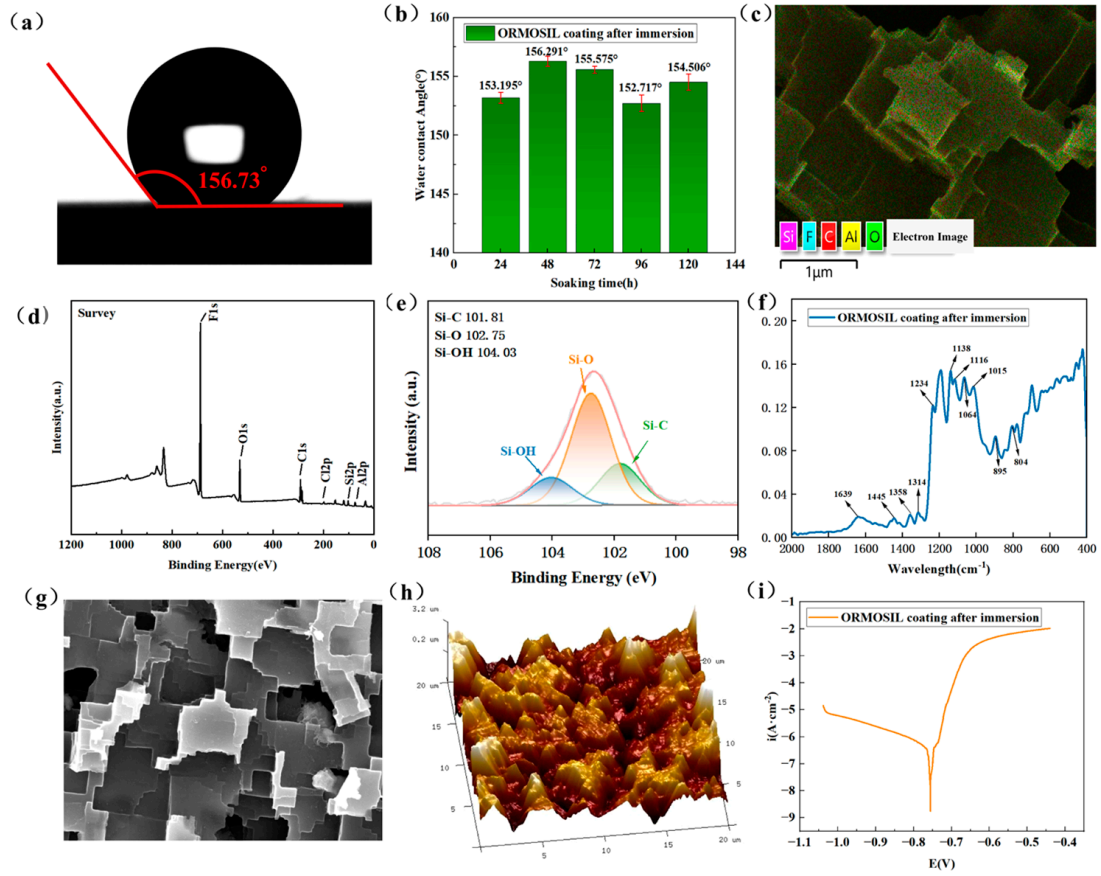


Figure 6. Characterization and performance tests of the ORMOSIL coating after jet fuel immersion: (**a**) water contact angle image showing the maximum value; (**b**) average water contact angle versus immersion time; (**c**) EDS elemental mapping; (**d**) XPS survey spectrum; (**e**) high-resolution Si 2p XPS spectrum; (**f**) FTIR spectrum; (**g**) SEM image; (**h**) AFM 3D surface morphology; and (**i**) polarization curve.

4. Conclusions

We developed a superhydrophobic surface on 6061 aluminum alloy using a two-step modification strategy, integrating $FeCl_3$-induced microstructuring with ORMOSIL-based surface functionalization to achieve low surface energy and superior water repellency. The aluminum surface was chemically etched with $FeCl_3$ to create hierarchical microstructures, followed by the sol–gel deposition of ORMOSIL using PFOTES and HDTMS precursors. Water contact angle measurements further revealed that the coating achieved a maximum contact angle of 161.44°, with water droplets forming nearly spherical shapes, indicating excellent water repellency and self-cleaning capability. Moreover, under simulated low-temperature icing conditions relevant to aviation fuel systems, the ORMOSIL coating exhibited outstanding low-temperature durability. Even in harsh cold environments, its micro/nanostructure and fluorinated low-surface-energy characteristics remained stable. Further characterization results revealed that the ORMOSIL-coated 6061 aluminum alloy surface exhibited distinct lamellar structures and granular deposits, forming an effective multiscale roughened architecture. AFM measurements showed an arithmetic average roughness of 0.654 nm and a root mean square roughness of 0.844 nm, indicating the successful construction of the micro/nanostructure. XPS and FTIR analyses confirmed the formation of a siloxane-based organic–inorganic ORMOSIL network containing Si-O-Si, Si-O-C/SiO_xC_y-related structures, residual Si-OH, C-F, and C-H groups. Potentiodynamic polarization tests conducted in 3.5 wt% NaCl solution demonstrated that the corrosion potential shifted positively from −0.723 V for the bare substrate to −0.652 V after coating,

indicating excellent corrosion resistance. This improvement is primarily attributed to the dense siloxane network and the hydrophobic barrier properties of the coating. Compared with the untreated and etched-only samples, the ORMOSIL-coated surface exhibited significantly enhanced electrochemical stability, confirming its potential as a protective material for aviation and other corrosive environments.

In the jet fuel immersion test, the performance of the ORMOSIL superhydrophobic coating exhibited a slight decline over time. However, even after 120 h of continuous immersion, the coating maintained excellent superhydrophobic and hydrophobic properties, demonstrating strong fuel resistance and long-term stability. To further evaluate its chemical and structural integrity, the coating was subjected to post-immersion characterization. XPS and FTIR analyses revealed that key functional groups such as -CF_2, -CF_3, and Si-O-Si remained present, with no significant changes in the characteristic absorption peaks, confirming the chemical stability of the coating. In addition, surface wettability tests indicated that the contact angle remained at a high level, suggesting that its water-repellent performance was largely unaffected. SEM and AFM analyses further confirmed that the micro/nanostructured morphology of the coating remained intact, with no signs of collapse or delamination. In summary, the ORMOSIL-based superhydrophobic coating demonstrated excellent structural integrity, chemical stability, and surface durability after 120 h of jet fuel immersion, indicating its strong potential for long-term application in aviation fuel systems.

Supplementary Materials: The following supporting information can be downloaded at https://www.mdpi.com/article/10.3390/cryst16070449/s1.

Author Contributions: Conceptualization, X.L. and H.W.; methodology, H.S. and J.R.; software, X.H.; validation, R.L. and Y.W.; formal analysis, X.L.; investigation, H.S., J.R. and X.H.; resources, L.Z.; data curation, R.L.; writing—original draft preparation, X.L.; writing—review and editing, H.W. and L.Z.; visualization, Y.W.; supervision, H.W.; project administration, H.W.; funding acquisition, X.L. and H.W. All authors have read and agreed to the published version of the manuscript.

Funding: This research was funded by the Key Research and Development Program of Sichuan Province, grant number 2025YFHZ0024, and the Fundamental Research Funds for the Central Universities, grant number 26CAFUC03054.

Data Availability Statement: The data presented in this study are available in the article and Supplementary Materials.

Conflicts of Interest: The authors declare no conflict of interest.

References

1. Weller, A.S. *Thermal Stress, Protection and Survival*; CRC Press: Boca Raton, FL, USA, 2025; pp. 224–239.
2. Rezvani Rad, M. Application of Thermally-Sprayed Coatings as Heat Tracers for Carbon Steel Pipes to Mitigate the Effect of Ice Accumulation and Freezing Damage. Ph.D. Thesis, University of Alberta, Edmonton, AB, Canada, 2020.
3. Wang, J.; Tao, Z.; Yang, R.; Shan, D.; Wang, W. A review of aircraft fire accident investigation techniques: Research, process, and cases. *Eng. Fail. Anal.* **2023**, *153*, 107558. [CrossRef]
4. He, H.; Guo, Z. Superhydrophobic materials used for anti-icing Theory, application, and development. *Iscience* **2021**, *24*, 103357. [CrossRef] [PubMed]
5. Zhang, W.; Wang, D.; Sun, Z.; Song, J.; Deng, X. Robust superhydrophobicity: Mechanisms and strategies. *Chem. Soc. Rev.* **2021**, *50*, 4031–4061. [CrossRef] [PubMed]
6. Liu, K.; Yao, X.; Jiang, L. Recent developments in bio-inspired special wettability. *Chem. Soc. Rev.* **2010**, *39*, 3240–3255. [CrossRef] [PubMed]
7. Dash, S.; Mishra, S.; Patel, S.; Mishra, B.K. Organically modified silica: Synthesis and applications due to its surface interaction with organic molecules. *Adv. Colloid Interface Sci.* **2008**, *140*, 77–94. [CrossRef] [PubMed]
8. Figueira, R.B.; Silva, C.J.R.; Pereira, E.V. Organic-inorganic hybrid sol-gel coatings for metal corrosion protection: A review of recent progress. *J. Coat. Technol. Res.* **2015**, *12*, 1–35.

9. Smitha, V.S.; Syamili, S.S.; Mohamed, A.P.; Nair, B.N.; Hareesh, U.S. ORMOSIL-ZrO_2 hybrid nanocomposites and coatings on aluminium alloys for corrosion resistance; a sol-gel approach. *New J. Chem.* **2018**, *42*, 10337–10347. [CrossRef]
10. Metroke, T.L.; Gandhi, J.S.; Apblett, A. Corrosion resistance properties of Ormosil coatings on 2024-T3 aluminum alloy. *Prog. Org. Coat.* **2004**, *50*, 231–246. [CrossRef]
11. Cui, J.; Jiang, D.; Xing, Z.; Yang, G. Study on the separation mechanism of icing adhesion and fracture on the surface of 6061 aluminum alloy. *Case Stud. Therm. Eng.* **2025**, *65*, 105620. [CrossRef]
12. Wang, H.; Dai, D.; Wu, X. Fabrication of superhydrophobic surfaces on aluminum. *Appl. Surf. Sci.* **2008**, *254*, 5599–5601. [CrossRef]
13. Bai, Y.; Zhang, H.; Shao, Y.; Zhang, H.; Zhu, J. Recent progresses of superhydrophobic coatings in different application fields: An overview. *Coatings* **2021**, *11*, 116. [CrossRef]
14. Ge, Y.; Cheng, J.; Xue, L.; Zhang, B.; Zhang, P.; Cui, X.; Hong, S.; Wua, Y.; Zhang, X.; Liang, X. Durability and corrosion behaviors of superhydrophobic amorphous coatings: A contrastive investigation. *RSC Adv.* **2022**, *12*, 32813–32824. [CrossRef] [PubMed]
15. Wankhede, R.G. Development of Hydrophobic Inorganic-Organic Hybrid Sol-Gel Coatings on Aluminium Using Nano-Particles. Ph.D. Thesis, IIT Bombay, Bombay, India, 2013.
16. Zhang, P.; Lv, F.Y. A review of the recent advances in superhydrophobic surfaces and the emerging energy-related applications. *Energy* **2015**, *82*, 1068–1087. [CrossRef]
17. Chen, Z.; Li, S.; Hihara, L.H. Microstructure, mechanical properties and corrosion of friction stir welded 6061 Aluminum Alloy. *arXiv* **2015**, arXiv:1511.05507.
18. Wang, J.; Ma, W.; Xin, G.; Pan, Y.; Zhang, Z.; Sun, Y. Preparation of dense modified nanosilica superhydrophilic coatings on aluminum alloy surfaces by adjusting amino groups. *Ceram. Int.* **2023**, *49*, 16123–16136. [CrossRef]
19. Saleema, N.; Sarkar, D.K.; Paynter, R.W.; Gallant, D.; Eskandarian, M. A simple surface treatment and characterization of AA 6061 aluminum alloy surface for adhesive bonding applications. *Appl. Surf. Sci.* **2012**, *261*, 742–748. [CrossRef]
20. Li, J.; Bai, H.; Feng, Z. Advances in the modification of silane-based sol-gel coating to improve the corrosion resistance of magnesium alloys. *Molecules* **2023**, *28*, 2563. [CrossRef] [PubMed]
21. More, A.P.; Mhaske, S.T. Chemical modification of silane-based coating with inhibitor for anticorrosive application. *Arab. J. Sci. Eng.* **2016**, *41*, 2239–2248.
22. Sano, K.; Kanematsu, H.; Tanaka, T. Overview of silane-based polymer coatings and their applications. In *Industrial Applications for Intelligent Polymers and Coatings*; Springer International Publishing: Cham, Switzerland, 2016; pp. 493–509.
23. Jesson, D.A. The Interaction of Nano-Composite Particles with a Polyester Resin and the Effect on Mechanical Properties. Ph.D. Thesis, University of Surrey, Guildford, UK, 2005.
24. Zhang, L.; Zhang, J.; Liu, R. Organic-inorganic hybrid sol-gel coatings for corrosion protection of aluminum alloys. *Surf. Innov.* **2016**, *4*, 51–69. [CrossRef]
25. Greczynski, G.; Haasch, R.T.; Hellgren, N.; Lewin, E.; Hultman, L. X-ray photoelectron spectroscopy of thin films. *Nat. Rev. Methods Prim.* **2023**, *3*, 40. [CrossRef]
26. Meyer, H.M., III; Sabau, A.S.; Daniel, C. Surface chemistry and composition-induced variation of laser interference-based surface treatment of Al alloys. *Appl. Surf. Sci.* **2019**, *489*, 893–904. [CrossRef]
27. Xian, A.; Wei, C.; Tang, Z.; Wang, Q.; Han, Z.; Song, X. Fluorinated LDHs for selective sorption of PFOS: Unveiling the roles of increased hydrophobicity and FF interactions. *Sep. Purif. Technol.* **2025**, *362*, 131851. [CrossRef]
28. Yi, B.; Wang, S.; Hou, C.; Huang, X.; Cui, J.; Yao, X. Dynamic siloxane materials: From molecular engineering to emerging applications. *Chem. Eng. J.* **2021**, *405*, 127023. [CrossRef]
29. Allen, D.M.; Almond, H.J.A. Characterisation of aqueous ferric chloride etchants used in industrial photochemical machining. *J. Mater. Process. Technol.* **2004**, *149*, 238–245. [CrossRef]
30. Li, X.; Yang, J.; Wang, J.; Chang, X.; Xu, J.; Wu, Z. A stable super-amphiphilic surface created from superhydrophobic silica/epoxy coating by low-temperature plasma-treatment. *Surf. Eng.* **2021**, *37*, 1282–1289. [CrossRef]
31. Van de Grampel, R.D. Surfaces of Fluorinated Polymer Systems. Ph.D. Thesis, Technische Universiteit Eindhoven, Eindhoven, The Netherlands, 2002.
32. Gong, L.; Wu, F.; Yang, W.; Chang, X.; Xu, J.; Wu, Z. Unraveling the hydrophobic interaction mechanisms of hydrocarbon and fluorinated surfaces. *J. Colloid Interface Sci.* **2023**, *635*, 273–283. [CrossRef] [PubMed]
33. Smith, B.C. *Fundamentals of Fourier Transform Infrared Spectroscopy*; CRC Press: Boca Raton, FL, USA, 2011.
34. Smith, A.L. Infrared spectra-structure correlations for organosilicon compounds. *Spectrochim. Acta* **1960**, *16*, 87–105. [CrossRef]
35. Gurav, A.B.; Guo, Q.; Tao, Y.; Mei, T.; Wang, Y.; Wang, D. Durable, robust and free-standing superhydrophobic poly (vinyl alcohol-co-ethylene) nanofiber membrane. *Mater. Lett.* **2016**, *182*, 106–109. [CrossRef]
36. Ji, W.; Wang, Z.; Ma, J.; Gong, J. Hydrothermal synthesis of boehmite on alumina membranes for superhydrophobic surfaces. *Surf. Eng.* **2016**, *32*, 102–107. [CrossRef]
37. Smith, B.C. *Infrared Spectral Interpretation: A Systematic Approach*; CRC Press: Boca Raton, FL, USA, 2018.
38. Socrates, G. *Infrared and Raman Characteristic Group Frequencies: Tables and Charts*; John Wiley & Sons: Hoboken, NJ, USA, 2004.

39. Li, L.; Li, B.; Dong, J.; Zhang, J. Roles of silanes and silicones in forming superhydrophobic and superoleophobic materials. *J. Mater. Chem. A* **2016**, *4*, 13677–13725. [CrossRef]
40. Mahmood, S. Mechanistic Understanding of Aluminium Alloy 6063 Corrosion in Product Store Environments. Ph.D. Thesis, The University of Manchester, Manchester, UK, 2020.
41. Feng, L.; Li, S.; Li, Y.; Li, H.; Zhang, L.; Zhai, J.; Song, Y.; Liu, B.; Jiang, L.; Zhu, D. Super-hydrophobic surfaces: From natural to artificial. *Adv. Mater.* **2002**, *14*, 1857–1860. [CrossRef]
42. Balaskas, A.C.; Kartsonakis, I.A.; Snihirova, D.; Montemor, M.F.; Kordas, G. Improving the corrosion protection properties of organically modified silicate-epoxy coatings by incorporation of organic and inorganic inhibitors. *Prog. Org. Coat.* **2011**, *72*, 653–662. [CrossRef]
43. Pan, R.; Cai, M.; Liu, W.; Luo, X.; Chen, C.; Zhang, H.; Zhong, M. Extremely high Cassie-Baxter state stability of superhydrophobic surfaces via precisely tunable dual-scale and triple-scale micro-nano structures. *J. Mater. Chem. A* **2019**, *7*, 18050–18062. [CrossRef]
44. Lee, J.Y.; Lee, E. Crystallographic orientation-dependent corrosion behavior of aluminum under residual stress. *Mater. Charact.* **2023**, *205*, 113310. [CrossRef]
45. Kruszelnicki, M.; Kowalczuk, P.B.; Polowczyk, I. Three-phase contact formation between an air bubble and solid surfaces with different hydrophobicity degrees in liquid. *Colloids Surf. A Physicochem. Eng. Asp.* **2023**, *676*, 132067. [CrossRef]
46. Liu, M.; Wang, S.; Jiang, L. Nature-inspired superwettability systems. *Nat. Rev. Mater.* **2017**, *2*, 17036. [CrossRef]
47. George, J.E.; Chidangil, S.; George, S.D. Recent progress in fabricating superaerophobic and superaerophilic surfaces. *Adv. Mater. Interfaces* **2017**, *4*, 1601088. [CrossRef]
48. Li, X.; Lin, X.; Wu, Y.; Zhang, Z.; Hu, T.; Jiang, L.; Xiao, T.; Tan, X. Superhydrophobic surface with good mechanical robustness and stable Cassie-Baxter state throughout freezing and thawing processes. *Surf. Interfaces* **2025**, *56*, 105619. [CrossRef]
49. Kung, C.H.; Sow, P.K.; Zahiri, B.; Mérida, W. Assessment and interpretation of surface wettability based on sessile droplet contact angle measurement: Challenges and opportunities. *Adv. Mater. Interfaces* **2019**, *6*, 1900839. [CrossRef]
50. Josyula, T.; Kumar Malla, L.; Thomas, T.M.; Kalichetty, S.S.; Sinha Mahapatra, P.; Pattamatta, A. Fundamentals and applications of surface wetting. *Langmuir* **2024**, *40*, 8293–8326. [CrossRef] [PubMed]
51. Law, K.Y.; Zhao, H. *Surface Wetting: Characterization, Contact Angle, and Fundamentals*; Springer: Cham, Switzerland, 2016.
52. Wang, X.; Feng, J.I.; Bai, Y.; Zhang, Q.; Yin, Y. Synthesis, properties, and applications of hollow micro-/nanostructures. *Chem. Rev.* **2016**, *116*, 10983–11060. [CrossRef] [PubMed]
53. Raimondo, M.; Blosi, M.; Caldarelli, A.; Guarini, G.; Veronesi, F. Wetting behavior and remarkable durability of amphiphobic aluminum alloys surfaces in a wide range of environmental conditions. *Chem. Eng. J.* **2014**, *258*, 101–109. [CrossRef]
54. Kang, H.E.; Kim, S.H.; Choi, J.H.; Kim, D.J.; Yoon, Y.S. Selective etching-induced surface modifications of FeCrAl alloy bipolar plates: Mechanisms for enhanced corrosion resistance and hydrophobicity. *Chem. Eng. J.* **2024**, *493*, 152409. [CrossRef]
55. Li, F.M.; Huang, L.; Zaman, S.; Guo, W.; Liu, H.; Guo, X.; Xia, B.Y. Corrosion chemistry of electrocatalysts. *Adv. Mater.* **2022**, *34*, 2200840. [CrossRef]
56. Uc-Fernández, E.; González-Sánchez, J.; Ávila-Ortega, A.; Pérez-Padilla, Y.; Cervantes-Uc, J.M.; Reyes-Trujeque, J.; Talavera-Pech, W.A. Anticorrosive properties of a superhydrophobic coating based on an ORMOSIL enhanced with MCM-41-HDTMS nanoparticles for metals protection. *J. Coat. Technol. Res.* **2023**, *20*, 347–357.
57. Wu, C.; Hou, D.; Wang, P.; Li, M.; Xu, H.; Han, S. Investigation of polysiloxane coatings with two-components for synergistic improved corrosion resistance of cementitious materials. *Constr. Build. Mater.* **2024**, *449*, 138142. [CrossRef]
58. Chen, L.; Xu, J.; Luo, X.; Liu, Z.; Wang, B.; Song, Q.; Cai, Y.; Wan, Y.; Gao, X.; Li, C. Micro/nano manufacturing aircraft surface with anti-icing and deicing performances: An overview. *Nanotechnol. Rev.* **2023**, *12*, 20230105. [CrossRef]
59. Chen, J.; Yi, J.; Ji, Y.; Zhao, B.; Ji, Y.; Li, G.; An, T. Enhanced H-abstraction contribution for oxidation of xylenes via mineral particles: Implications for particulate matter formation and human health. *Environ. Res.* **2020**, *186*, 109568. [CrossRef] [PubMed]
60. Shahien, M.; Shinoda, K.; Akedo, J. Hybrid aerosol deposition as an outstanding prospective for dense barrier ceramic coatings deposition on different substrates. In *ITSC2022*; ASM International: Materials Park, OH, USA, 2022; pp. 709–715.
61. Gujba, A.K.; Mahdipoor, M.S.; Medraj, M. Water droplet impingement erosion performance of WC-based coating sprayed by HVAF and HVOF. *Wear* **2021**, *484*, 203904. [CrossRef]
62. Li, X.; He, X. Preparation of Superhydrophobic Coating with Silica Powder on Flexible Substrates. *Nanosci. Nanotechnol. Lett.* **2018**, *10*, 554–558. [CrossRef]
63. Wang, Q.; Cui, Z.; Xiao, Y.; Chen, Q. Stable highly hydrophobic and oleophilic meshes for oil–water separation. *Appl. Surf. Sci.* **2007**, *253*, 9054–9060. [CrossRef]
64. Jiang, L.; Park-Lee, K.J.; Clinton, R.M.; Tang, Z.; Breedveld, V.; Hess, D.W. Mechanical durability of liquid repellent coatings. *Surf. Coat. Technol.* **2017**, *328*, 182–191. [CrossRef]
65. Hakimian, A.; Nazifi, S.; Ghasemi, H. Durability assessment of icephobic coatings. In *Ice Adhesion: Mechanism, Measurement and Mitigation*; John Wiley & Sons, Inc.: Hoboken, NJ, USA, 2020; pp. 521–545.

66. Wu, Y.L.; She, W.; Shi, D.; Jiang, T.; Hao, T.H.; Liu, J.; Zhang, Q.; You, J.; Li, R.Y. An extremely chemical and mechanically durable siloxane bearing copolymer coating with self-crosslinkable and anti-icing properties. *Compos. Part B Eng.* **2020**, *195*, 108031. [CrossRef]
67. Du, Y.J.; Damron, M.; Tang, G.; Zheng, H.; Chu, C.J.; Osborne, J.H. Inorganic/organic hybrid coatings for aircraft aluminum alloy substrates. *Prog. Org. Coat.* **2001**, *41*, 226–232. [CrossRef]
68. Innocenzi, P. Infrared spectroscopy of sol–gel derived silica-based films: A spectra-microstructure overview. *J. Non-Cryst. Solids* **2003**, *316*, 309–319. [CrossRef]
69. Múgica-Vidal, R.; Alba-Elías, F.; Sainz-García, E.; Pantoja-Ruiz, M. Hydrophobicity attainment and wear resistance enhancement on glass substrates by atmospheric plasma-polymerization of mixtures of an aminosilane and a fluorocarbon. *Appl. Surf. Sci.* **2015**, *347*, 325–335. [CrossRef]
70. Múgica-Vidal, R.; Alba-Elías, F.; Sainz-García, E.; Ordieres-Meré, J. Atmospheric plasma-polymerization of hydrophobic and wear-resistant coatings on glass substrates. *Surf. Coat. Technol.* **2014**, *259*, 374–385. [CrossRef]
71. Saget, M.; Nuns, N.; Supiot, P.; Foissac, C.; Bellayer, S.; Dourgaparsad, K.; Royoux, P.; Delaplace, G.; Thomy, V.; Coffinier, Y.; et al. Ultra-hydrophobic biomimetic transparent bilayer thin film deposited by atmospheric pressure plasma. *Surf. Interfaces* **2023**, *42*, 103398. [CrossRef]
72. Farahat, M.; Sobhy, A.; Sanad, M.M. Superhydrophobic magnetic sorbent via surface modification of banded iron formation for oily water treatment. *Sci. Rep.* **2022**, *12*, 11016. [CrossRef] [PubMed]
73. Deng, W.; Long, M.; Zhou, Q.; Wen, N.; Deng, W. One-step preparation of superhydrophobic acrylonitrile-butadiene-styrene copolymer coating for ultrafast separation of water-in-oil emulsions. *J. Colloid Interface Sci.* **2018**, *511*, 21–26. [CrossRef] [PubMed]
74. Du, Z.; Ding, P.; Tai, X.; Pan, Z.; Yang, H. Facile preparation of Ag-coated superhydrophobic/superoleophilic mesh for efficient oil/water separation with excellent corrosion resistance. *Langmuir* **2018**, *34*, 6922–6929. [CrossRef] [PubMed]

Disclaimer/Publisher's Note: The statements, opinions and data contained in all publications are solely those of the individual author(s) and contributor(s) and not of MDPI and/or the editor(s). MDPI and/or the editor(s) disclaim responsibility for any injury to people or property resulting from any ideas, methods, instructions or products referred to in the content.